Journal of Hazardous Materials 380 (2019) 120814

Contents lists available at ScienceDirect

Journal of Hazardous Materials

journal homepage: www.elsevier.com/locate/jhazmat

New insights into the synergistic effect of active radicals and adsorptive ability on the photodegradation of gaseous acetaldehyde over reduced graphene Oxide/P25 composite

Qinglong Zeng[a,b], Xiaofeng Xie[a,*], Xiao Wang[a], Guanhong Lu[a], Haiwei Li[c], Shun Cheng Lee[c], Jing Sun[a,*]

[a] Shanghai Institute of Ceramics, Chinese Academy of Sciences, Shanghai 200050, China
[b] University of Chinese Academy of Sciences, 19 Yuquan Road, Beijing 100049, China
[c] Department of Civil and Environmental Engineering, The Hong Kong Polytechnic University, Hung Hom, Hong Kong, China

GRAPHICAL ABSTRACT

New insights into reduced graphene oxide/P25 composite and its photocatalytic performance

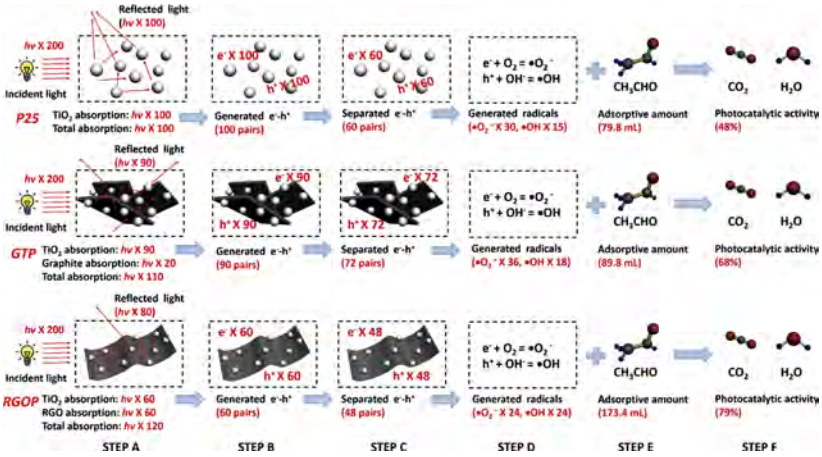

ARTICLE INFO

Editor: Danmeng Shuai

Keywords:
Photothermal conversion
Active radicals
Adsorptive ability
Gaseous acetaldehyde

ABSTRACT

Although coupling reduced graphene oxide (RGO) with TiO_2 is believed to enhance the photocatalysis through the light utilization, studies on its photothermal conversion effect are rarely reported. Herein, RGOP (reduced graphene oxide/P25) was synthesized to explore roles of the enhanced light adsorption and photothermal conversion in the photocatalytic process. It was found that although RGOP had increased absorbance, it actually possessed lower available light utilization compared with P25. In the synergistic effect of available light utilization, transfer resistance and hydrophilicity, RGOP exhibited less superoxide radicals but more hydroxyl radicals. In the presence of scavenger experiments, $\cdot O_2^-$ was proved to play the predominant role in the photocatalytic process, while $\cdot$OH was the secondary one. In comparison to P25, the change of active radicals of RGOP

* Corresponding Authors.
E-mail addresses: xxfshcn@163.com (X. Xie), jingsun@mail.sic.ac.cn (J. Sun).

https://doi.org/10.1016/j.jhazmat.2019.120814
Received 1 April 2019; Received in revised form 12 June 2019; Accepted 22 June 2019
Available online 10 July 2019

was adverse to its photocatalysis. However, due to the superior adsorptive property of RGOP, it exhibited higher photocatalytic activity than P25. The improved photocatalytic activity of RGOP was ascribed to its superior adsorptive ability aside from active radicals ($^{\cdot}O_2$-, $^{\cdot}OH$).

1. Introduction

More and more contaminant appears in the atmosphere because of the rapid development of human society (Yang et al., 2015; Trapalis et al., 2016; Liu et al., 2018a). It is of great importance to deal with this tough issue. Among so many solutions, photocatalysis has attracted much attention due to its thorough purification for diverse pollutants compared with other feasible strategies (Zhang et al., 2015; Wang et al., 2017; Sun et al., 2014; Razzaq et al., 2016). TiO_2 is regarded as the most promising photocatalyst owing to its low price, good stability and nontoxicity (Liu et al., 2018a; Pan et al., 2013). However, the poor adsorption of organic pollutants, the fast recombination of e^--h^+ pairs and the poor light-harvesting capacity inhibit its photocatalytic performance extremely.

Incorporating two-dimensional materials with TiO_2 is an effective way to elevate its photocatalytic activity. It is well recognized that RGO is one of the most popular two-dimensional materials in photocatalytic research field. Therefore, many efforts about coupling RGO with TiO_2 have been done to increase the photocatalytic performance (Hu et al., 2016; Pan et al., 2015; Xu et al., 2016a, b). It turns out that RGO in the composites does have a positive effect on the photocatalysis because of its large specific surface area, great electric conductivity and excellent visible light response. That is, the addition of RGO in the composites usually brings three benefits: the increased adsorption of pollutants, the improved separation of e^--h^+ pairs and the enhanced light-capture ability (Zhang et al., 2017; Rathod et al., 2016; Ton et al., 2018; Wu et al., 2016). To achieve these advantages, the RGO used here has to be the single-layer (or few-layers) RGO. However, for the practical situation, the single-layer (or few-layers) RGO only exists in the supernatant, which takes only a small part of the product. In other words, most of the obtained RGO was actually in the form of multi-layers. While the excessive thickness of carbon layers would shield the absorption of light (Liu et al., 2018b). Then, if the applied RGO was not single-layer (or few-layers) RGO but mainly in the form of multi-layers, its inhibited effect on light must be taken into account. Nevertheless, there are few articles focusing on this issue (Xu et al., 2016b; Liu et al., 2018b; Wang et al., 2012).

In this paper, the multi-layers RGO/P25 composite was synthesized to explore this question. The results revealed the composite still have better photocatalytic performance compared with pure P25. The addition of multi-layers RGO made the composite have the increased adsorption of pollutants, the decreased transfer resistance and more hydroxyl radicals, which is similar with previous report (Ton et al., 2018; Jo et al., 2017; Cruz-Ortiz et al., 2017). However, it accompanies with several negative effects such as the lower available light utilization, the declined photo-current density and less superoxide radicals. Briefly, the addition of RGO brought both positive and negative effect on the photocatalytic performance of RGOP.

2. Experimental section

2.1. Materials

Commercial P25 sample was obtained from Degussa. Graphite (325 mesh) was supplied by Alfa Aesar. Sodium borohydride ($NaBH_4$) was purchased from Aladdin Industrial Corporation. p-benzoquinone was produced by Aladdin Industrial Corporation, and 2,2,6,6-tetramethyl-1-piperidinyloxy was also supplied by this company. DI was used in the whole experimental process.

2.2. The synthesis of RGOP and GTP

First, graphite oxide were prepared from graphite by Hummers' method. Subsequently, 0.117 g graphite oxide was dispersed into

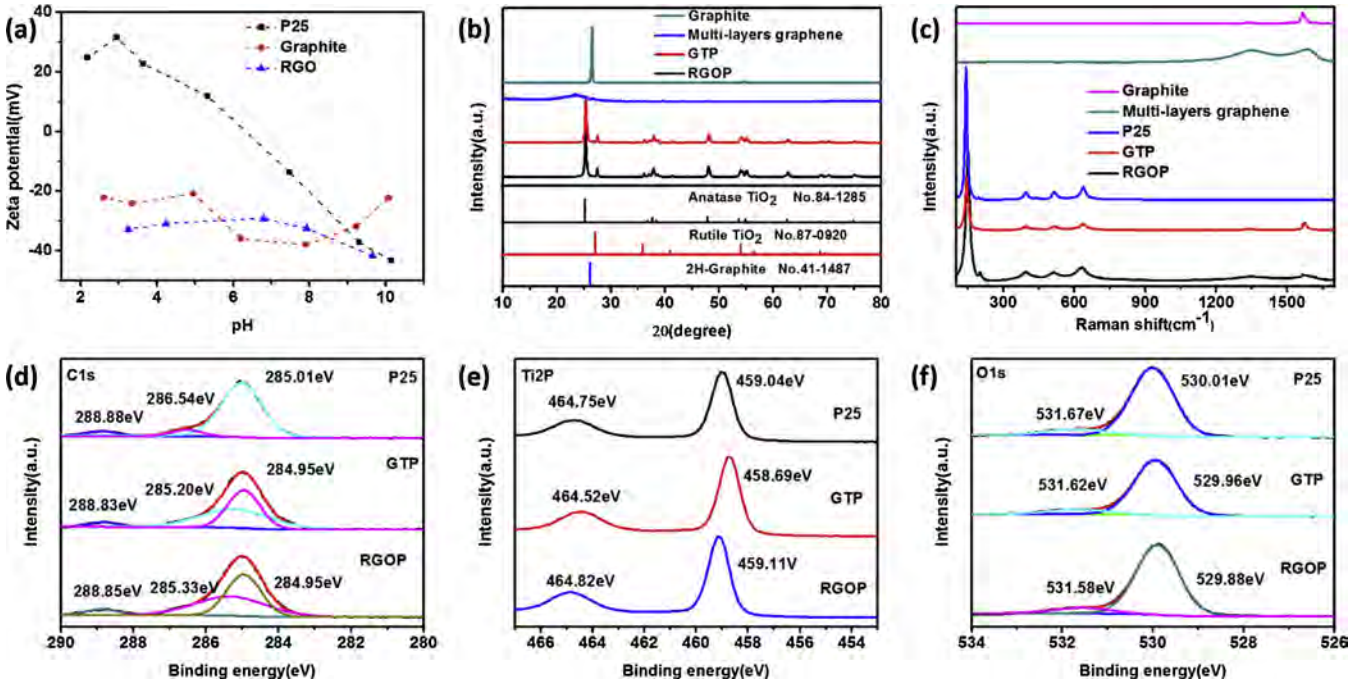

Fig. 1. (a) Zeta potential of P25, graphite and RGO (b) XRD spectra of the obtained samples (c) Raman spectra of the as-prepared samples (d–f) XPS spectra of C1s, Ti2p, O1s, respectively.

200 mL ethanol with sonication, and then 0.23 g reductant $NaBH_4$ was added, followed by magnetic stirring for 24 h at room temperature. Multi-layers RGO was obtained by washing with deionized water for three times.

Approximately 3.5 mg multi-layers RGO was dispersed in 50 mL DI water (pH = 3) through sonication. Approximately 350 mg P25 was also dispersed in 50 mL deionized water (the pH was also 3), and then P25 dispersion was added slowly into the above mixture. The obtained sample was noted as RGOP, where RGO stands for multi-layers RGO and P for P25. Similarly, GTP was synthesized by using 3.5 mg graphite, where GT stands for graphite and P for P25. As shown in Fig. 1a, P25 was positive charge when the pH approximated to 3, whereas graphite or RGO was negative charge. By means of electrostatic interaction, graphite blocks or RGO nanosheets could be wrapped by P25 nanoparticles closely. The mass ratio of RGO (or graphite) in RGOP (or GTP) was 1 wt%.

2.3. Characterizations

XRD spectra were collected by a D8 ADVANCE instrument. A 950 spectrometer was used to conduct UV–vis tests. BET results were recorded on a ASAP 3000 equipment. Photoluminescence (PL) tests were carried out through LS55. SEM images were collected on Magellan 400. XPS experiments were conducted on a 310 F instrument. Temperature programmed desorption (TPD) analysis was performed in ChemiSorb PCA-1200, Builer, China. Zeta potential tests were conducted on a zetaPLUS analysis meter. Wetting angle tests were recorded on a DSA100 by spinning the sample onto a FTO glass (KRUSS GmbH). Electron spin resonance (ESR) tests were recorded on a JES-FA200 equipment. Photo-current response and electrochemical impedance spectroscopy tests were recored on a CHI660D equipment.

2.4. Evaluation of photocatalytic performance

The photocatalytic performance was evaluated through the removal ratio of flowing gaseous acetaldehyde. Fig. S1 was the corresponding meaurement setup. Fig. S2 was the corresponding adsorption-desorption curves. The original concentration of gaseous acetaldehyde was about 500 ppm, and the flux rate was about 20 sccm. The removal ratio (Y) was noted as $Y = (C_0 - C)/C_0 \times 100\%$, here C_0 was the original concentration, while C stood for the real-time concentration of gaseous acetaldehyde.

2.5. Photothermal conversion tests

Photothermal conversion tests were conducted on a home-made set-up. Fig. S3 was the simplified schematic, an AM1.5 G irradiation with (or without) a 420 nm filter was applied as light source. 0.2 g sample powder was firstly placed into the quartz tube, and then the temperature sensors were inserted into the above powder, followed by the upper opening of the tube sealed. The original environment temperature for three samples (P25, GTP, RGOP) was controlled at 27 °C. After all this, the light source was turned on, and the data were obtained every 30 s.

2.6. Trapping experiments for reactive species idenfication

0.01 g PBQ (P-benzoquinone) was mixed with 0.1 g photocatalyst to quench superoxide radicals, and expressed as "X + PBQ". 0.01 g TEMPO (2,2,6,6-tetramethyl-1-piperidinyloxy) was mixed with 0.1 g photocatalyst to quench hydroxyl radicals, and expressed as "X + TEMPO". 0.01 g PTFE was also mixed with 0.1 g photocatalyst, and expressed as "X + No scavenger", which served as a blank experiment. Here, X represented P25, GTP or RGOP.

3. Results and evaluations

3.1. Characterizations of elemental composition and morphologies

The phase structures of P25, graphite, RGO, GTP and, RGOP were investigated by XRD and Raman analysis. As shown in Fig. 1b, the peak located at $2\theta = 26.4°$ of graphite was ascribed to (002) facet of 2H-graphite and the corresponding layer spacing was 0.34 nm (JCPDS No.41-1487) (Asgar et al., 2018). As for RGO, a broad peak centered at $2\theta = 24.8°$ was observed, assigned to an interlayer spacing of 0.37 nm (Trapalis et al., 2016). It is not surprising that both anatase and rutile phase TiO_2 existed in the XRD patterns of GTP and RGOP (Fig. 1b), because commercial P25 itself was consisted of 70% anatase and 30%

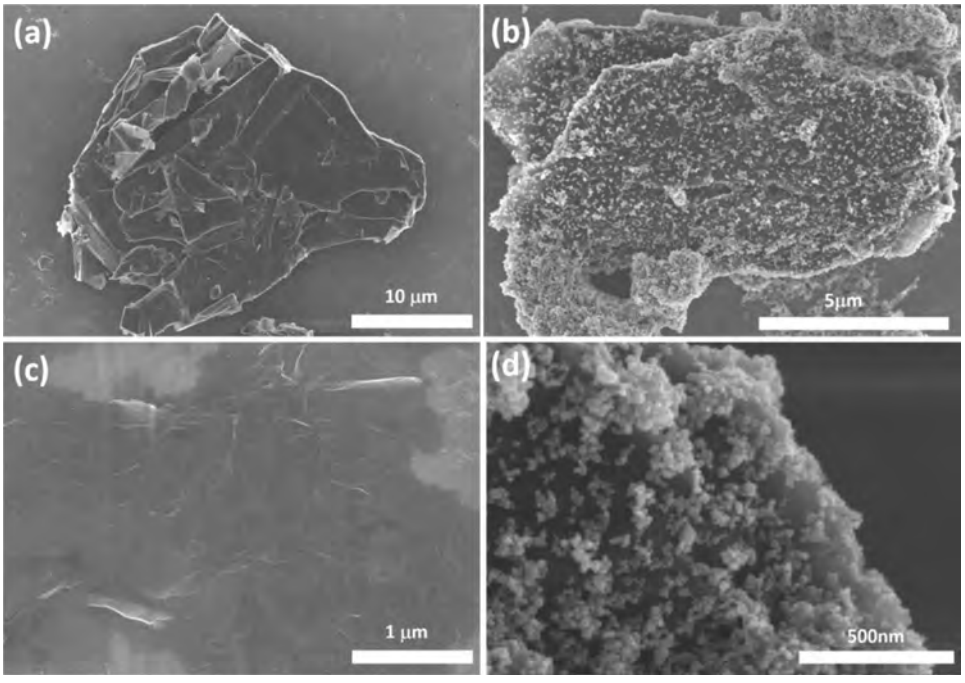

Fig. 2. SEM images of (a) bare graphite (b) GTP (c) bare RGO (d) RGOP.

rutile TiO_2. However, no graphite or RGO characteristic peaks were found in the composites, this should be due to the small content of graphite or RGO in the composites (1% weight ratio). It is well-accepted that XRD detection sensitivity is about 5%, that is why they could not be detected by XRD measurements. Raman test is a powerful technique to prove the existence of C species because of its higher sensitivity compared with XRD. In Raman spectra (Fig. 1c), five active Raman peaks (144, 199, 396, 513, 636 cm^{-1}) were observed, which belonged to anatase TiO_2 (Zhang et al., 2015; Purbia et al., 2017). Furthermore, two typical Raman peaks, the D band centered at 1344 cm^{-1} and the G band at 1580 cm^{-1}, are found in bare RGO and RGOP. Similarly, the typical G band settled at 1566 cm^{-1} was found in graphite and GTP (Asgar et al., 2018). Therefore, the existence of graphite or RGO in the composites (GTP, RGOP) was proved by means of XRD and Raman.

The elemental composition and the chemical status of samples were tested by XPS measurements. The C1s XPS spectra of P25 can be deconvoluted into three peaks (Fig. 1d), which can be assigned to sp2 bonded carbon (C—C, 285.01 eV), epoxy/hydroxyls (C–O, 286.54 eV), carboxyl (O—C = O, 288.88 eV) (Rajender et al., 2018). P25 did not contain any C species, three C XPS peaks here mainly belonged to adventitious C which derived from the XPS instrument itself, and it was inevitable. Compared with the XPS peak of P25 (286.54 eV, Fig. 1d), there is an obvious shift of 0.3 eV for GTP and 0.2 eV for RGOP. The existence of graphite or RGO in the compsites (GTP and RGOP) accounted for these differences. The Ti2p XPS peaks (Fig. 1e, P25) located at 459.04 eV and 464.75 eV was ascribed to Ti^{4+}, no characteristic peaks of Ti^{3+} or Ti^{2+} were found (Wang et al., 2017). While for GTP, compared with P25, the Ti2p3/2 of Ti^{4+} had a 0.3 eV shift, this is a proof of close coupling between graphite and P25 (Liu et al., 2018a). As for O1s of P25 and GTP (Fig. 1f), the peaks (530.01 eV and 529.96 eV) were ascribed to the Ti-O bonds, and the peaks (531.67 eV and 531.62 eV) were assigned to the Ti—OH bonds (Purbia et al., 2017). There is a 0.1 eV shift in the O1s of RGOP, this could be ascribed to the residual oxygen-containing functional groups in RGO, such as hydroxy and carboxy (Ton et al., 2018). In addition to XPS, FTIR can also give some useful information about elemental composition. As suggested by FTIR spectra (Fig. S4), there is almost no difference in the characteristic functional groups of the samples (P25, GTP and RGOP), which should be ascribed to the small loading content of graphite and RGO in the composites. The band centered at 3429 cm^{-1} was due to the active modes of O—H, which was associated with absorbed water (Zhou et al., 2011). While the band fixed at 1639 cm^{-1} resulted from the vibrations of absorbed water. 519 cm^{-1} and 661 cm^{-1} were due to the stretching vibrations of Ti—O and Ti—O—Ti (Zhang et al., 2018). Briefly, the result verified the presence of graphite or RGO in the composites, which were consistent with the above-mentioned XRD and Raman tests.

The morphology of bare graphite, bare RGO, GTP and RGOP was observed by SEM images. As reveled by Fig. 2a, graphite was actually hierarchal stacking structure with rough appearance, which was consisted of many thick graphite blocks irregularly. As shown in Fig. 2c, many relatively smooth and thin nanosheets were seen clearly, which is obtained RGO. Whatever it is GTP (Fig. 2b) or RGOP (Fig. 2d), the surface of graphite or RGO was surrounded by multiple P25 nanoparticles tightly. In addition, it is worth noticing that the P25 nanoparticles were in well-dispersion, which benefited from the opposite electrical property carried during the synthesis process. As shown in Fig. 1a (Zeta potential), P25 was with positive charge at pH 3, meanwhile both graphite and RGO were negatively charged. Consequently, through electrostatic interaction between P25 and graphite or RGO, P25 was attached on their surface evenly and closely. In a word, graphite or RGO was seen clearly in the composites (GTP, RGOP) with the help of SEM, which was in good accordance with the results of Raman and XPS analysis.

3.2. The relationship between light-harvesting and light utilization

The light-harvesting capacity is an important influence factor of photocatalytic perfomance. Generally speaking, the more light absorption should be beneficial to the better photocatalysis (Pan et al., 2015; Xu et al., 2016b; Tan et al., 2015). As shown in Fig. 3a, RGOP or GTP exhibited higher UV–vis absorbance than P25 when the wavelength was greater than 420 nm. In addition, an obvious red-shift of absorption edge of GTP or RGOP was observed in contrast to that of P25. Here, it was easy to associate better photocatalysis with GTP or RGOP because of their excellent light absorption when the wavelength was greater than 420 nm. As shown in Fig. 3c, a 420 nm filter was applied when the irradiation time came to 65 min, then the light with wavelength < 420 nm can not take effect. After that, the photocatalytic performance of the three catalysts (P25, GTP and RGOP) quickly dropped to 0%. Namely, although GTP and RGOP had stronger light absorption compared with P25, they did not have better photocatalytic performance when the wavelength was greater than 420 nm. Therefore, it comes to an important truth that the apparent light-harvesting (UV–vis spectra) was not equal to the available light utilization in the photocatalytic process. Therefore, compared with P25, the increasing absorbance of GTP, RGOP should be due to their gradually blackened appearance (Fig. S5). Similarly, Fig. 3b is the PL spectra, the PL test results were not only related to recombination rate of electron-hole pairs but also the available light utilization. Therefore, UV–vis spectra and PL spectra can not represent the available light utilization and the separated electron-hole pairs completely.

Generally speaking, when a semiconductor is illuminated by light, there are three energy conversion paths for light: light reflection, photothermal conversion and available light utilization. Among them, light reflection was on the contrary of apparent light-harvesting (UV–vis spectra). Futhermore, apparent light-harvesting (UV–vis spectra) was also the sum of photothermal conversion and available light utilization. Compared with P25, the stronger absorbance of GTP or RGOP mainly resulted from the light above 420 nm. While as illustrated by Fig. 3c, the light absorbed by GTP or RGOP above 420 nm can not take effect, so it was not the available light utilization but turned into heat (Fig. 4a). Three photocatalysts had similar absorbance when

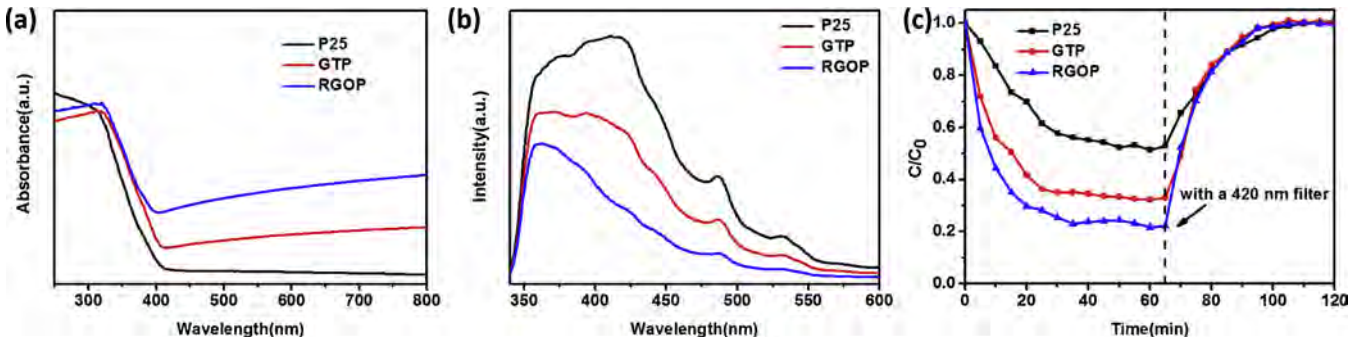

Fig. 3. (a) UV–vis spectra of P25, GTP, and RGOP (b) PL spectra of P25, GTP, and RGOP (c) The photocatalytic performance of P25, GTP, and RGOP for gaseous acetaldehyde (When the time came to 65 min, a 420 nm filter was applied).

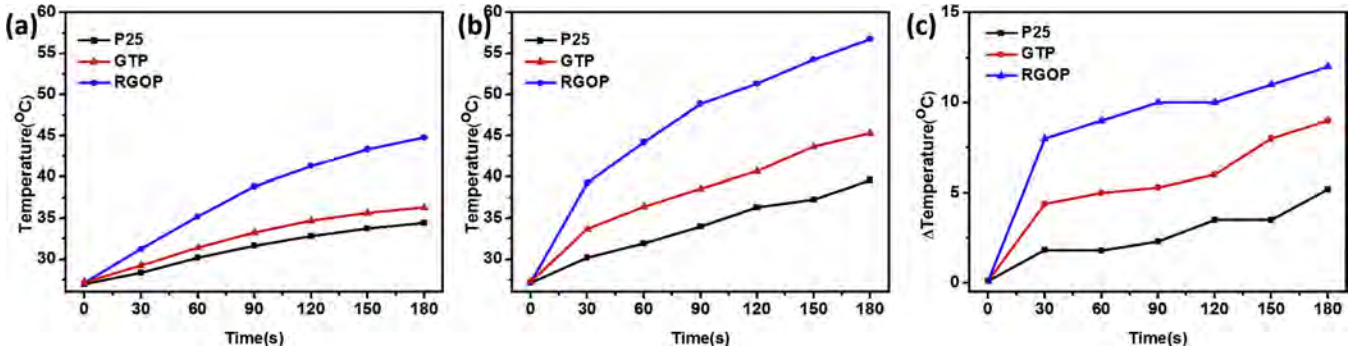

Fig. 4. (a) Photothermal conversion of of P25, GTP, and RGOP with a 420 nm filter (b) Photothermal conversion of of P25, GTP, and RGOP without a 420 nm filter (c) The temperature change of P25, GTP, and RGOP between without and with a 420 nm filter.

wavelength was below 420 nm (Fig. 3a). In other words, the available light utilization depended on the photothermal conversion of the light which wavelength was below 420 nm, and it could be calculated by the difference of the results of Fig. 4a and b. Consequently, the order of the available light utilization could be derived from the sequence of the photothermal conversion. The results of photothermal conversion were displayed in Fig. 4c, the photothermal conversion below 420 nm was in the following order: RGOP > GTP > P25. Therefore, the available light utilization of three photocatalysts was in the following order: P25 > GTP > RGOP. Namely, in GTP or RGOP, graphite or RGO absorbed lots of light, but it was mainly converted into heat (Liu et al., 2018b; Zhou et al., 2011). Briefly, these results can be summarized into one point: Coupling graphite or RGO with P25 improved their apparent light-harvesting because of their dark appearance (Fig. 3a, Fig. S5), but along with decreased available light utilization, and the order of available light utilization is P25 > GTP > RGOP.

3.3. The synergistic effect of available light utilization and transfer resistance on the separated amount of e^--h^+ pairs

Although the available light utilization of GTP and RGOP was worse than that of P25, while their photocatalytic performance (Fig. 3c) was better than P25. The reason was, in addition to the influence of available light utilization on photocatalytic performance, there were still some other influencing factors. The separated amount of electron-hole pairs would also affect the photocatalytic activity (Tang et al., 2018; Jiang et al., 2014; Chen et al., 2018). Under the stimulus of light, photoinduced e^--h^+ pairs were generated. Then, the generated e^--h^+ pairs would be separated, electrons would flow to the conduction band of TiO_2, and holes would be left in the valence band of TiO_2 (Soni et al., 2008). Therefore, the separated amount of e^--h^+ pairs was mainly related to two aspects. On the one hand, it depended on the generated e^--h^+ pairs, and the generated e^--h^+ pairs was consistent with the available light utilization. On the other hand, it would affect by the transfer resistance of charge. Therefore, electrochemical impedance spectroscopy (EIS) was utilized to evaluate the transfer resistance. As shown in Fig. 5a, the arc size of EIS curves reflected the transfer resistance of charge. The smaller arc size usually stood for the lower charge transfer resistance (Wang et al., 2013a; Li et al., 2013). P25 had the biggest arc compared with GTP or RGOP, which meant the slowest charge separation. While GTP or RGOP had the similar arc size, which was much smaller than that of P25. In other words, coupling graphite or RGO with P25 could decline the transfer resistance effectively.

We already knew that the available light utilization of three catalysts was in the order of P25 > GTP > RGOP, meanwhile the order of transfer resistance was P25 > GTP ≈ RGOP. Based on these relationships, it can be concluded that the separated amount of e^--h^+ pairs of GTP was more than that of RGOP. While it is a pity that no more conclusions could be drawn from these relationships. But fortunately, photo-current results were essentially the synergistic effect of available light utilization and transfer resistance. That is, the results of photo-current tests could represent the separated amount of e^--h^+ pairs basically (Xiang et al., 2011; Wang et al., 2013b). Therefore, photo-current tests were carried out to disclose the relationships of the separated amount of e^--h^+ pairs of P25, GTP and RGOP. As shown in Fig. 5b, GTP had the largest photo-current, while RGOP had the smallest photo-current. In other words, the separated amount of e^--h^+ pairs of GTP was more than that of RGOP, which was in good agreement with just-mentioned inference. For GTP and RGOP, they had similar transfer resistance (Fig. 5a) but with distinct available light utilization (Fig. 4c), so GTP had larger photo-current than RGOP (Fig. 5b). While the separated amount of e^--h^+ pairs of P25 was between that of GTP and RGOP, which was just a result of the synergistic effect of available light utilization and transfer resistance.

3.4. The formation of active radicals ($\cdot O_2^-$, $\cdot OH$) and their roles

ESR measurements were carried out to monitor the production of $\cdot O_2^-$ and $\cdot OH$. As shown in Fig. 6a, there were four typical bands of

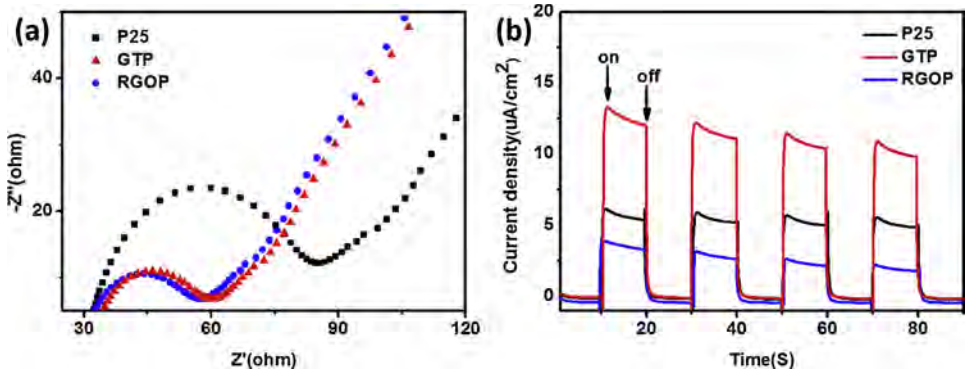

Fig. 5. (a) Electrochemical impedance spectroscopy tests of P25, GTP, and RGOP (d) Photo-current response of P25, GTP and, RGOP.

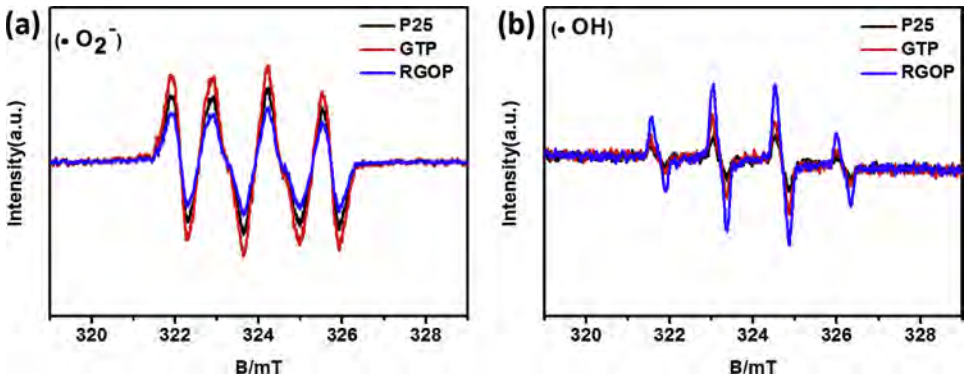

Fig. 6. (a) DMPO spin-trapping $^{\cdot}O_2^-$ ESR signal (b) DMPO spin-trapping $^{\cdot}OH$ ESR signal.

superoxide radicals (the area ration was about 1:1:1:1), and Fig. 6b is the hydroxyl radicals spectra with four characteristic bands (the area ration was about 1:2:2:1). As revealed in Fig. 6a, b, the ESR signals of $^{\cdot}O_2^-$ and $^{\cdot}OH$ of GTP were much stronger than that of P25. This should be related to the separated amount of e^--h^+ pairs, as shown in Fig. 5b, GTP had relative larger photo-current density compared with P25. And also, as displayed in Fig. 3c, more active radicals are beneficial to the improvement of photocatalytic performance (Zhang et al., 2016; Wang et al., 2016). While there was a different situation for RGOP (Fig. 6a, b), it possessed less superoxide radicals (Fig. 6a) but more hydroxyl radicals (Fig. 6b) in comparison to P25. In fact, it is no wonder that there was the less superoxide radicals in RGOP because of its smallest photo-current density (Fig. 5b). As for more hydroxyl radicals, it is well-recognized that the interaction between holes and water resulted in the production of $^{\cdot}OH$ (Peng et al., 2014; Lv et al., 2016; Ding et al., 2016). In this case, the hydrophilicity of the catalysts would also take a great effect on the generation of $^{\cdot}OH$. Therefore, wetting angle tests were applied to reflect the hydrophilicity of the catalysts. As shown in Fig. S6, P25 and GTP had the similar wetting angle, so the generation of their $^{\cdot}OH$ mainly depended on the photo-current density. With respect to RGOP, a very small wetting angle was observed compared with P25 or GTP. The generation of $^{\cdot}OH$ of RGOP was decided by not only photo-current density but also hydrophilicity, and then it (more $^{\cdot}OH$) made sense. However, it was difficult for us to judge whether this change (less $^{\cdot}O_2^-$ but more $^{\cdot}OH$) was beneficial to the photocatalysis of RGOP or not.

Consequently, it was of great importance to disclose the effect of superoxide and hydroxyl radicals. In order to understand the role of $^{\cdot}O_2^-$ and $^{\cdot}OH$, scavenger experiments were conducted. $^{\cdot}O_2^-$ and $^{\cdot}OH$ were quenched by using PBQ and TEMPO as the corresponding scavenger reagents (Zhang et al., 2016; Wang et al., 2016; Lv et al., 2016; Ding et al., 2016). As shown in Fig. 7, when $^{\cdot}O_2^-$ and $^{\cdot}OH$ were quenched, it was found that the corresponding photocatalytic activity differenced. The more the photocatalytic performance declined, the more important role the corresponding radicals played. Through the observation of Fig. 7a, b, and c, it could be concluded that, for three catalysts (P25, GTP and RGOP), $^{\cdot}O_2^-$ radicals played the predominant role compared with $^{\cdot}OH$ radicals in the photodecomposition of gaseous acetaldehyde. Based on this result, it could be stated that: compared with P25, GTP had more active radicals ($^{\cdot}O_2^-$, $^{\cdot}OH$) which are beneficial to the improvement of photocatalytic performance; while for RGOP, it had less superoxide radicals but more hydroxyl radicals in comparison to P25, which were disadvantageous for its photocatalysis owing to the verified predominant role of $^{\cdot}O_2^-$ radicals.

3.5. The adsorptive ability and its influence on photocatalysis

As shown in Fig. 3c, the photocatalytic performance of P25, GTP, and RGOP was 48%, 68%, and 79%, respectively. GTP did have the better photocatalytic activity than P25, while the photocatalysis of RGOP was not only higher than that of P25 but even better than that of GTP. For the photocatalysis of gaseous acetaldehyde, except for the impact of the active radicals, the adsorptive property of the catalysts was another significant influence factor on the photocatalytic activity since the adsorption of gaseous molecule was the prerequisite for photocatalytic reaction. The specific surface area of the catalysts was supplied by N_2 adsorption analysis. As listed in Table 1, the S_{BET} area of P25, GTP and RGOP was 63.9696 m^2/g, 58.0440 m^2/g, 69.8171 m^2/g, there was no distinct difference on their S_{BET} area. Compared with P25, the S_{BET} area of GTP did not decline significantly, meanwhile the S_{BET} area of RGOP did not increase sharply.

In fact, S_{BET} can only reflect the weak binding adsorption between catalysts and pollutants, such as physical adsorption, but cannot stand for the strong binding adsorption, such as chemical adsorption (Asgar et al., 2018). Temperature programmed desorption (TPD) analysis was applied to investigate the adsorptive property of catalysts (Mikhaylov et al., 2013; Luo et al., 2018). As shown in Fig. 8a, there were three kinds of peaks centered at different temperature, the TPD peak located at 200 °C was related to weak binding adsorption, and it had the lowest intensity compared with another two peaks. The order of its intensity

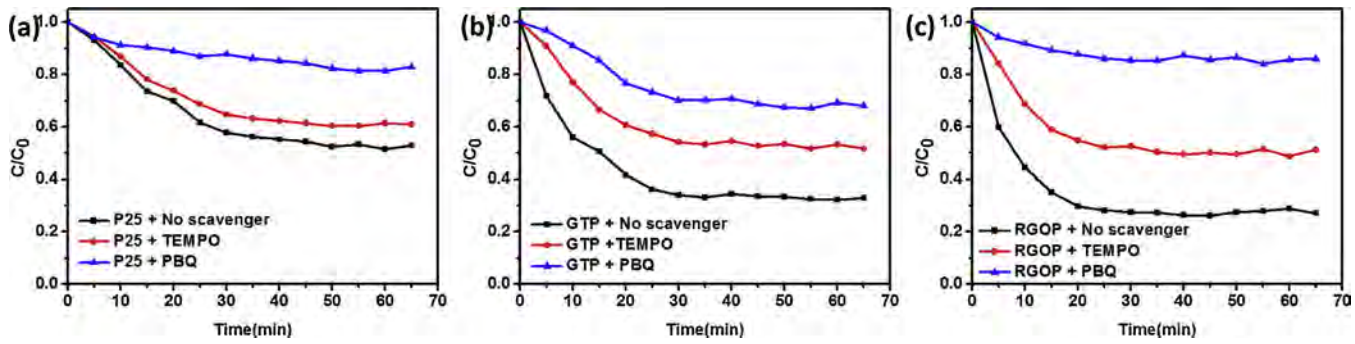

Fig. 7. (a) scavenger experiments of P25 (b) scavenger experiments of GTP (c) scavenger experiments of RGOP.

Table 1
S_{BET} and adsorptive property of P25, GTP, and RGOP (the adsorptive amount of acetaldehyde was obtained from Fig. 8b).

Sample	P25	GTP	RGOP
S_{BET} (m^2/g)	63.9696	58.0440	69.8171
Adsorptive amount of acetaldehyde (mL)	79.8	89.8	173.4

was in good accordance with the above S_{BET} results of three catalysts. Two other TPD peaks settled at 450 °C and 700 °C with higher intensity were observed, which could be ascribed to strong binding adsorption. The higher TPD intensity represented stronger adsorptive capacity. Namely, for the adsorption of acetaldehyde, strong binding adsorption was in the main form, while weak binding adsorption was in the secondary one. Furthermore, compared with P25 or GTP, RGOP had the largest adsorptive capacity in the whole TPD spectra, which should

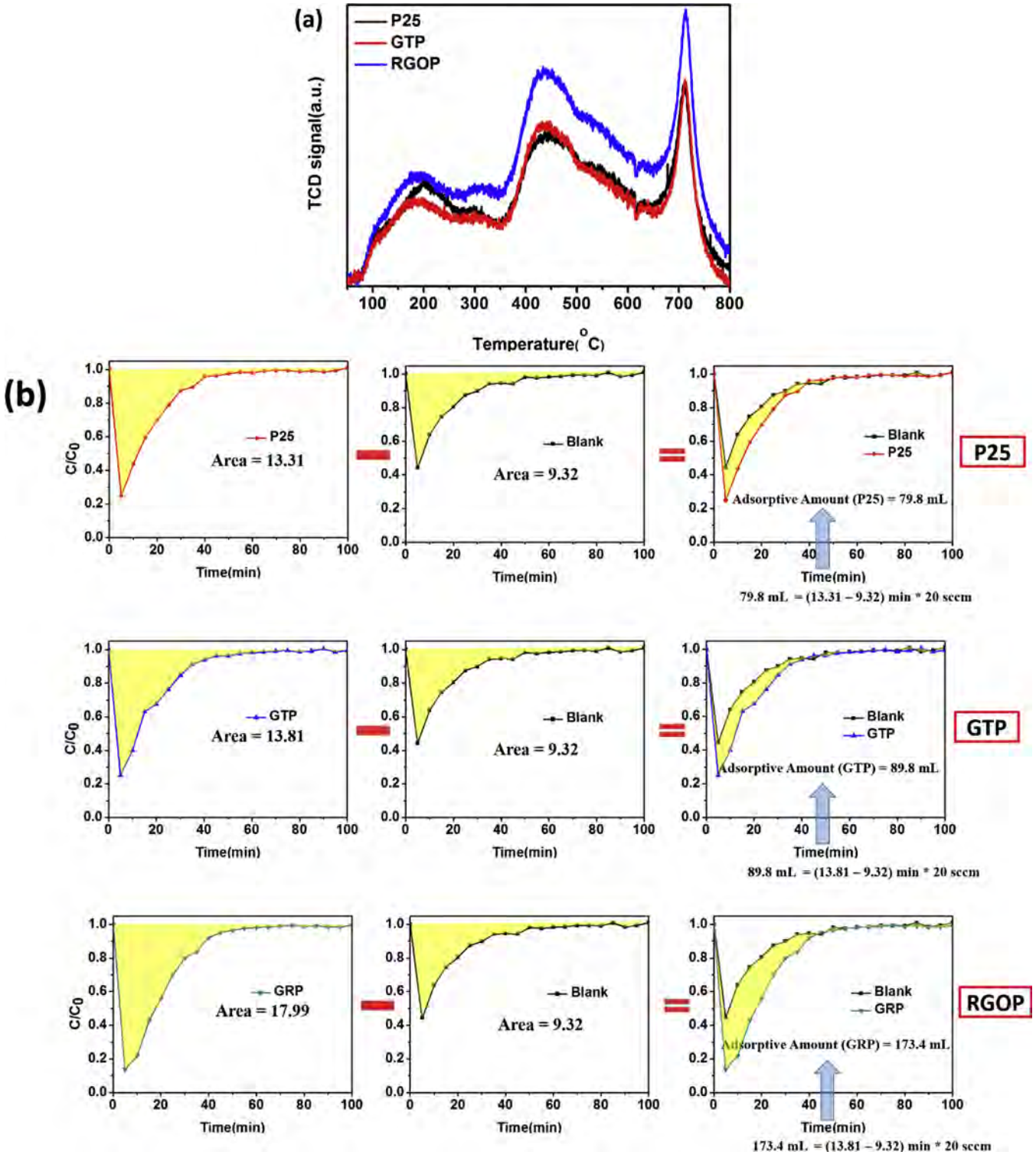

Fig. 8. (a) TPD tests of P25, GTP and RGOP by using 500 ppm acetaldehyde as the adsorptive gas with the temperature ranged from 50 °C to 800 °C (b) The adsorptive amount of acetaldehyde of P25, GTP, and RGOP.

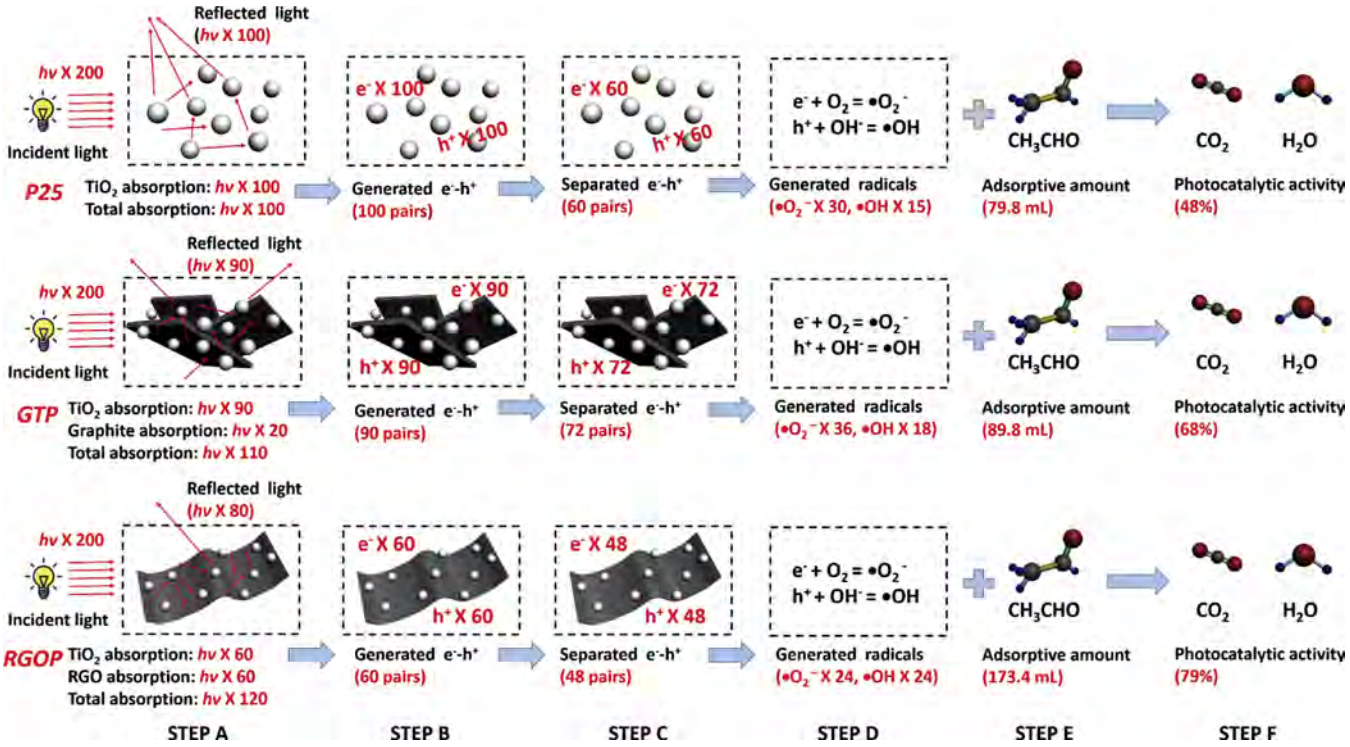

Fig. 9. Schemtic illustration of photocatalytic process from adsorbing light to photodegrading acetaldehyde into carbon dioxide and water *(Notes: the arabic numerals of STEP A–D did not stand for the specific numbers of anything mentioned in the picture, here it was used to explain the process more vividly).*

benefit from the close interaction between gaseous acetaldehyde and RGO. Besides, as displayed in Fig. S2, the specific adsorptive amount of acetaldehyde can be obtained. The area between adsorption-desorption curve and the straight line ($C/C_0 = 1$) could be obtain through mathematical integral (Fig. S2). The flow rate of acetaldehyde was 20 sccm. And then, the adsorptive amount of acetaldehyde can be worked out. The specific calculated progress was shown in Fig. 8b, the obtained results were listed in Table 1, and the adsorptive amount of gaseous acetaldehyde was 79.8 mL, 89.8 mL, 173.4 mL for P25, GTP, RGOP, respectively. The adsorptive capacity of RGOP was almost twice than that of P25 or GTP. Then, it was no wonder that why RGOP still had excellent photocatalytic performance compared with P25 or GTP. In other words, compared with P25 or GTP, though RGOP was with less superoxide radicals and more hydroxyl radicals which were harmful to the improvement of photocatalytic performance, while it had extremely high adsorptive ability for acetaldehyde, that is what made it exhibit outstanding photocatalysis. As for GTP, its adsorptive ability for acetaldehyde was near to that of P25, but it had more active radicals ($^{\cdot}O_2^-$, $^{\cdot}OH$), so it also had higher photocatalysis in comparison to P25.

Finally, the entire photocatalytic process was summarized as Fig. 9. When the photocatalysts were illuminated by light, there were three energy conversion paths for light: light reflection, photothermal conversion and available light utilization, which was STEP A. Under the stimulus of available light, the corresponding photoinduced e^--h^+ pairs were generated (STEP B). Then, the generated e^--h^+ pairs would undergo the separation process, and the separated e^--h^+ pairs depended on the available light utilization and the transfer resistance (STEP C). After that, the interaction between photoinduced electrons (holes) and oxygen (water) resulted in the production of $^{\cdot}O_2^-$ ($^{\cdot}OH$) (STEP D). STEP E was the adsoptive process between photocatalysts and gaseous acetaldehyde. At last, gaseous acetaldehyde would be decomposed into CO_2 and H_2O (STEP F).

4. Conclusions

Although GTP and RGOP had stronger absorbance compared with P25, they both possessed lower available light utilization. $^{\cdot}O_2^-$ was proved to play the predominant role in the photocatalytic process, while $^{\cdot}OH$ was the secondary one. Compared with P25, more active radicals ($^{\cdot}O_2^-$ and $^{\cdot}OH$) and similar adsorptive capacity of GTP accounted for its better photocatalytic performance. In terms of active radicals, RGOP which was with less superoxide radicals but more hydroxyl radicals should have worse activity. However, due to the superior adsorptive property of RGOP, it still exhibited higher photocatalytic activity than P25. The improved photocatalysis of GTP was mainly due to its more active radicals, and the superior adsorptive property of RGOP was mainly responsible for its elevated photocatalysis. This paper would cast more light on the thorough comprehension of the photocatalytic process.

Acknowledgements

This work was financially supported by the National Key Research and Development Program of China (2016YFA0203000), the NSFC-DFG bilateral organization program (51761135107) and Shanghai Sailing Program (18YF1426800).

Appendix A. Supplementary data

Supplementary material related to this article can be found, in the online version, at doi:https://doi.org/10.1016/j.jhazmat.2019.120814.

References

Asgar, H., Deen, K.M., Riaz, U., Rahman, Z.U., Shah, U.H., Haider, W., 2018. Synthesis of graphene via ultra-sonic exfoliation of graphite oxide and its electrochemical characterization. Mater. Chem. Phys. 206, 7–11.

Chen, L., Yang, S., Mu, L., Ma, P.C., 2018. Three-dimensional titanium dioxide/graphene hybrids with improved performance for photocatalysis and energy storage. J. Colloid Interface Sci. 512, 647–656.

Cruz-Ortiz, B.R., Hamilton, J.W.J., Pablos, C., Díaz-Jiménez, L., Cortés-Hernández, D.A., Sharma, P.K., Castro-Alférez, M., Fernández-Ibañez, P., Dunlop, P.S.M., Byrne, J.A., 2017. Mechanism of photocatalytic disinfection using titania-graphene composites under UV and visible irradiation. Chem. Eng. J. 316, 179–186.

Ding, X., Ho, W., Shang, J., Zhang, L., 2016. Self doping promoted photocatalytic removal of no under visible light with Bi_2MoO_6: indispensable role of superoxide ions. Appl. Catal. B 182, 316–325.
Hu, L., Zhang, Y., Zhang, S., Li, B., 2016. A transparent TiO_2–C@TiO_2–graphene free-standing film with enhanced visible light photocatalysis. RSC Adv. 6, 43098–43103.
Jiang, W., Zhang, M., Wang, J., Liu, Y., Zhu, Y., 2014. Dramatic visible activity in phenol degradation of TCNQ@TiO_2 photocatalyst with core–shell structure. Appl. Catal. B 160-161, 44–50.
Jo, W.-K., Kumar, S., Isaacs, M.A., Lee, A.F., Karthikeyan, S., 2017. Cobalt promoted TiO_2/GO for the photocatalytic degradation of oxytetracycline and Congo Red. Appl. Catal. B 201, 159–168.
Li, G., Wu, L., Li, F., Xu, P., Zhang, D., Li, H., 2013. Photoelectrocatalytic degradation of organic pollutants via a CdS quantum dots enhanced TiO_2 nanotube array electrode under visible light irradiation. Nanoscale 5, 2118–2125.
Liu, H., Chen, Z., Zhang, L., Zhu, D., Zhang, Q., Luo, Y., Shao, X., 2018a. Graphene grown on anatase–TiO_2 nanosheets: enhanced photocatalytic activity on basis of a well-controlled interface. J. Phys. Chem. C 122, 6388–6396.
Liu, F., Feng, N., Yang, L., Wang, Q., Xu, J., Deng, F., 2018b. Enhanced photocatalytic performance of carbon-coated TiO_{2-x} with surface-active carbon species. J. Phys. Chem. C 122, 10948–10955.
Luo, J., Kamasamudram, K., Currier, N., Yezerets, A., 2018. NH_3-TPD methodology for quantifying hydrothermal aging of Cu/SSZ-13 SCR catalysts. Chem. Eng. Sci. 190, 60–67.
Lv, K., Guo, X., Wu, X., Li, Q., Ho, W., Li, M., Ye, H., Du, D., 2016. Photocatalytic selective oxidation of phenol to produce dihydroxybenzenes in a TiO_2/UV system: Hydroxyl radical versus hole. Appl. Catal. B 199, 405–411.
Mikhaylov, R.V., Lisachenko, A.A., Shelimov, B.N., Kazansky, V.B., Martra, G., Coluccia, S., 2013. FTIR and TPD study of the room temperature interaction of a NO–oxygen mixture and of NO_2 with titanium dioxide. J. Phys. Chem. C 117, 10345–10352.
Pan, X., Zhang, N., Fu, X., Xu, Y.-J., 2013. Selective oxidation of benzyl alcohol over TiO_2nanosheets with exposed {001} facets: catalyst deactivation and regeneration. Appl. Catal. A Gen. 453, 181–187.
Pan, D., Jiao, J., Li, Z., Guo, Y., Feng, C., Liu, Y., Wang, L., Wu, M., 2015. Efficient separation of electron–hole pairs in graphene quantum dots by TiO_2 heterojunctions for dye degradation. ACS Sustain. Chem. Eng. 3, 2405–2413.
Peng, W.C., Wang, X., Li, X.Y., 2014. The synergetic effect of MoS_2 and graphene on Ag_3PO_4 for its ultra-enhanced photocatalytic activity in phenol degradation under visible light. Nanoscale 6, 8311–8317.
Purbia, R., Borah, R., Paria, S., 2017. Carbon-doped mesoporous anatase TiO_2 multi-tubes nanostructures for highly improved visible light photocatalytic activity. Inorg. Chem. 56, 10107–10116.
Rajender, G., Kumar, J., Giri, P.K., 2018. Interfacial charge transfer in oxygen deficient TiO_2-graphene quantum dot hybrid and its influence on the enhanced visible light photocatalysis. Appl. Catal. B 224, 960–972.
Rathod, P.B., Nemade, K.R., Waghuley, S.A., 2016. Improvement in photovoltaic performance of TiO_2 nanoparticles by decoration of graphene nanosheets with spherical TiO_2 nanoparticles. Mater. Lett. 169, 118–121.
Razzaq, A., Grimes, C.A., In, S.-I., 2016. Facile fabrication of a noble metal-free photocatalyst: TiO_2 nanotube arrays covered with reduced graphene oxide. Carbon 98, 537–544.
Soni, S.S., Henderson, M.J., Bardeau, J.-F., Gibaud, A., 2008. Visible-light photocatalysis in titania-based mesoporous thin films. Adv. Mater. 20, 1493–1498.
Sun, H., Liu, S., Liu, S., Wang, S., 2014. A comparative study of reduced graphene oxide modified TiO_2, ZnO and Ta_2O_5 in visible light photocatalytic/photochemical oxidation of methylene blue. Appl. Catal. B 146, 162–168.
Tan, L.-L., Ong, W.-J., Chai, S.-P., Mohamed, A.R., 2015. Noble metal modified reduced graphene oxide/TiO_2 ternary nanostructures for efficient visible-light-driven photoreduction of carbon dioxide into methane. Appl. Catal. B 166-167, 251–259.
Tang, B., Chen, H., Peng, H., Wang, Z., Huang, W., 2018. Graphene modified TiO_2 composite photocatalysts: mechanism, progress and perspective. Nanomaterials (Basel) 8.
Ton, N.N.T., Dao, A.T.N., Kato, K., Ikenaga, T., Trinh, D.X., Taniike, T., 2018. One-pot synthesis of TiO_2/graphene nanocomposites for excellent visible light photocatalysis based on chemical exfoliation method. Carbon 133, 109–117.
Trapalis, A., Todorova, N., Giannakopoulou, T., Boukos, N., Speliotis, T., Dimotikali, D., Yu, J., 2016. TiO_2/graphene composite photocatalysts for NOx removal: A comparison of surfactant-stabilized graphene and reduced graphene oxide. Appl. Catal. B 180, 637–647.
Wang, W., Yu, J., Xiang, Q., Cheng, B., 2012. Enhanced photocatalytic activity of hierarchical macro/mesoporous TiO_2–graphene composites for photodegradation of acetone in air. Appl. Catal. B 119-120, 109–116.
Wang, Y., Wang, Q., Zhan, X., Wang, F., Safdar, M., He, J., 2013a. Visible light driven type II heterostructures and their enhanced photocatalysis properties: a review. Nanoscale 5, 8326–8339.
Wang, Z., Yang, C., Lin, T., Yin, H., Chen, P., Wan, D., Xu, F., Huang, F., Lin, J., Xie, X., Jiang, M., 2013b. Visible-light photocatalytic, solar thermal and photoelectrochemical properties of aluminium-reduced black titania. Energy Environ. Sci. 6, 3007.
Wang, Z., Huang, Y., Ho, W., Cao, J., Shen, Z., Lee, S.C., 2016. Fabrication of $Bi_2O_2CO_3$ /g-C_3N_4 heterojunctions for efficiently photocatalytic NO in air removal: in-situ self-sacrificial synthesis, characterizations and mechanistic study. Appl. Catal. B 199, 123–133.
Wang, L., Zhao, Y., Zhang, J., 2017. Photochemical removal of SO_2 over TiO_2-based nanofibers by a dry photocatalytic oxidation process. Energy Fuels 31, 9905–9914.
Wu, D., Yi, M., Duan, H., Xu, J., Wang, Q., 2016. Tough TiO_2-rGO-PDMAA nanocomposite hydrogel via one-pot UV polymerization and reduction for photodegradation of methylene blue. Carbon 108, 394–403.
Xiang, Q., Yu, J., Jaroniec, M., 2011. Enhanced photocatalytic H_2-production activity of graphene-modified titania nanosheets. Nanoscale 3, 3670–3678.
Xu, Y., Mo, Y., Tian, J., Wang, P., Yu, H., Yu, J., 2016a. The synergistic effect of graphitic N and pyrrolic N for the enhanced photocatalytic performance of nitrogen-doped graphene/TiO_2 nanocomposites. Appl. Catal. B 181, 810–817.
Xu, C., He, X., Wang, C., Chen, X., Yuan, R., Dai, W., 2016b. Introduction of holes into graphene sheets to further enhance graphene–TiO_2 photocatalysis activities. RSC Adv. 6, 84068–84073.
Yang, X., Qin, J., Jiang, Y., Chen, K., Yan, X., Zhang, D., Li, R., Tang, H., 2015. Fabrication of P25/Ag_3PO_4/graphene oxide heterostructures for enhanced solar photocatalytic degradation of organic pollutants and bacteria. Appl. Catal. B 166–167, 231–240.
Zhang, H., Guo, L.H., Wang, D., Zhao, L., Wan, B., 2015. Light-induced efficient molecular oxygen activation on a Cu(II)-grafted TiO_2/graphene photocatalyst for phenol degradation. ACS Appl. Mater. Interfaces 7, 1816–1823.
Zhang, Z., Xu, M., Ho, W., Zhang, X., Yang, Z., Wang, X., 2016. Simultaneous excitation of PdCl2 hybrid mesoporous g-C_3N_4 molecular/solid-state photocatalysts for enhancing the visible-light-induced oxidative removal of nitrogen oxides. Appl. Catal. B 184, 174–181.
Zhang, S., Xu, J., Hu, J., Cui, C., Liu, H., 2017. Interfacial growth of TiO_2-rGO composite by pickering emulsion for photocatalytic degradation. Langmuir 33, 5015–5024.
Zhang, Y., Cui, W., An, W., Liu, L., Liang, Y., Zhu, Y., 2018. Combination of photoelectrocatalysis and adsorption for removal of bisphenol A over TiO_2-graphene hydrogel with 3D network structure. Appl. Catal. B 221, 36–46.
Zhou, K., Zhu, Y., Yang, X., Jiang, X., Li, C., 2011. Preparation of graphene–TiO_2 composites with enhanced photocatalytic activity. New J. Chem. 35, 353–359.